

Supplementary material for
**Synchronization phenomena observed in
glacial-interglacial cycles simulated in an Earth
system model of intermediate complexity**

Takahito Mitsui* *et al.*

May 31, 2023

*Corresponding author. Email: takahito321@gmail.com

This PDF file includes:

Figs. S1 to S13
References

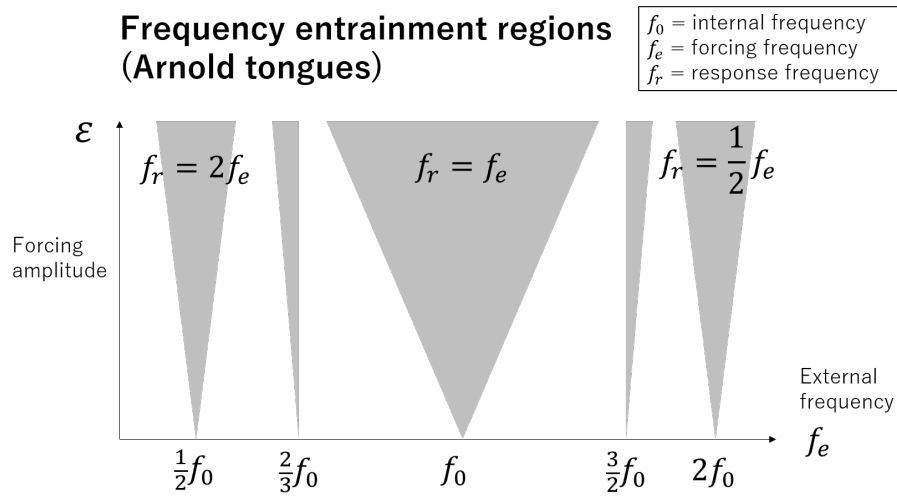


Figure S1. Schematic of frequency entrainment (synonymously, synchronization). If a self-sustained oscillator with internal frequency f_0 is subject to an external forcing with frequency f_e , the frequency of response oscillations f_r can be entrained at f_e . This frequency entrainment occurs within a finite range of frequency detuning $f_e - f_0$, which is wider if the forcing amplitude is larger. This region is called *Arnold tongue* (gray triangular region). If the internal frequency f_0 is far away from the external frequency f_e but close to one of simple harmonics $(m/n)f_e$ ($m, n \in \mathbb{N}$), the higher-order $m : n$ entrainment can occur at $(m/n)f_e$. In particular, the frequency entrainment at $(1/n)f_e$ is called the *subharmonic entrainment*. However, the higher-order frequency-entrainment has narrower entrainment regions and is less likely than a lower-order one. Infinitely many Arnold tongues exist between major tongues, but are not shown here. See [1] for more details.

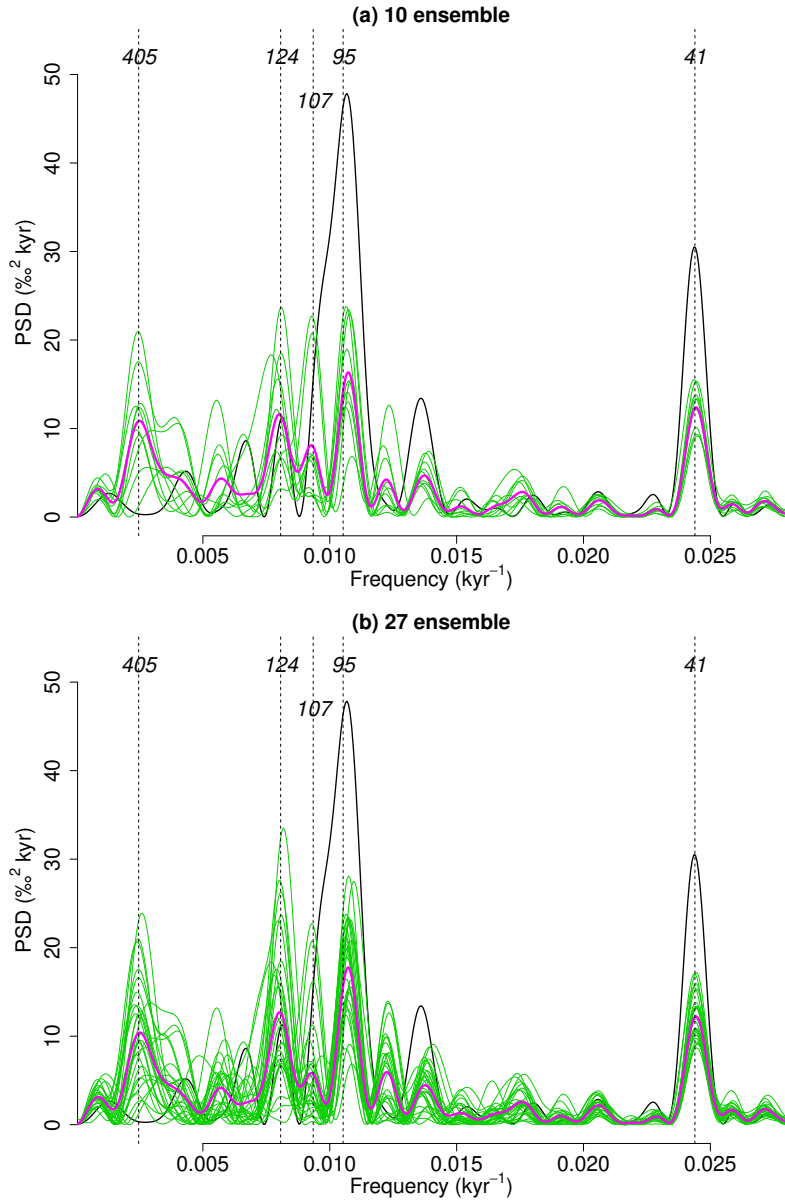


Figure S2. Enlarged version of the power spectral densities (PSD) of Fig. 2(d) for 10 $\delta^{18}\text{O}$ series simulated by CLIMBER-2 under the post-MPT background condition and the 1 Myr-to-present astronomical forcing (green). The magenta line shows the average of ten individual PSD. The then simulations start from different initial times between 1.1 Myr and 1.2 Myr; i.e., from different initial orbital configurations. The black line corresponds to the observed record [2]. (b) Same as (a) but with 27 simulated $\delta^{18}\text{O}$ series. Dashed lines are shown at major astronomical periodicities [3]. The 95-kyr power tends to be strongest statistically. For some realizations, a noticeable peak arises at 107-kyr periodicity, which may be interpreted as a higher-order combination tone of 95-kyr and 405-kyr eccentricity periodicities ($1/107 \simeq 1/95 - 1/(2 \times 405)$) [4].

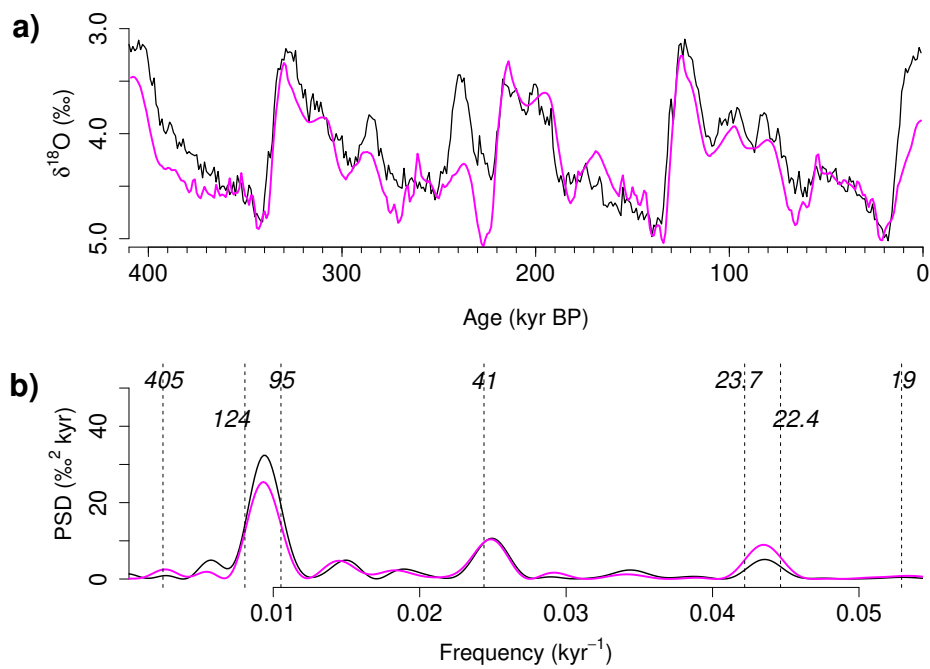


Figure S3. (a) Comparison between the $\delta^{18}\text{O}$ record [2] and the CLIMBER-2 simulation started from an interglacial level at 410 kyr BP. (b) Corresponding power spectral densities (PSD). Both have a stronger ~ 100 -kyr power and a substantially weaker 405-kyr power. Thus the relatively strong 405-kyr power in the 1 Myr simulations in Fig. 2(d) can be partly due to the absence of termination around 430 kyr BP.

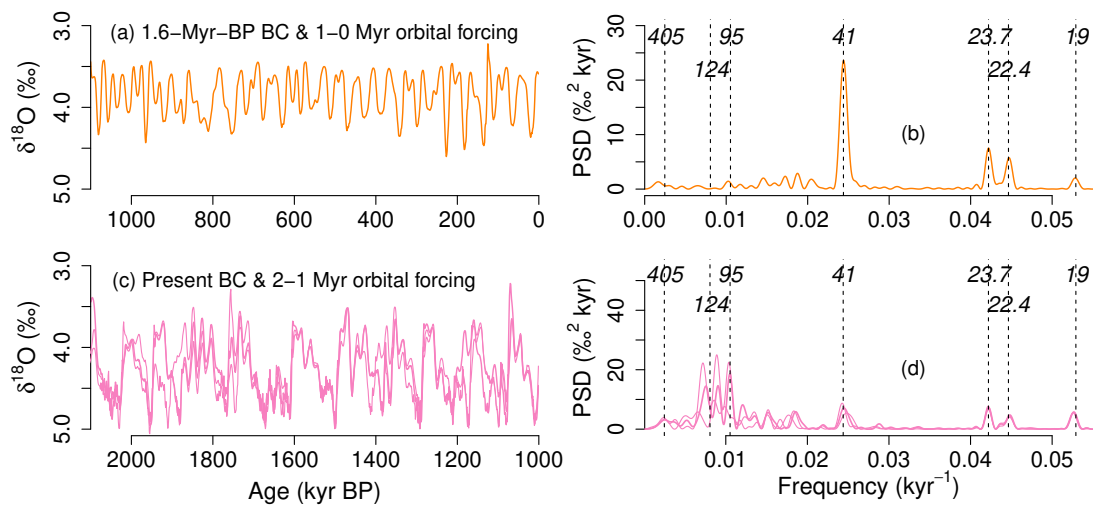


Figure S4. CLIMBER-2 simulations replacing the pre-MPT astronomical forcing with the post-MPT forcing and vice versa: (a) Simulated $\delta^{18}\text{O}$ under the fixed background condition (BC) at 1.6 Myr BP and the astronomical forcing [3] over 1–0 Myr BP. (b) The power spectral density (PSD) corresponding to the $\delta^{18}\text{O}$ series in (a). The vertical dashed lines and associated numbers in italics indicate the major astronomical periodicities [3]. (c) Simulated $\delta^{18}\text{O}$ under the fixed BC at 0 Myr BP and the astronomical forcing over 2–1 Myr BP. (d) The power spectral density (PSD) corresponding to the $\delta^{18}\text{O}$ series in (c). These results demonstrate that the MPT simulated in CLIMBER-2 cannot be produced by changes in the astronomical forcing alone, consistently with the previous work [5].

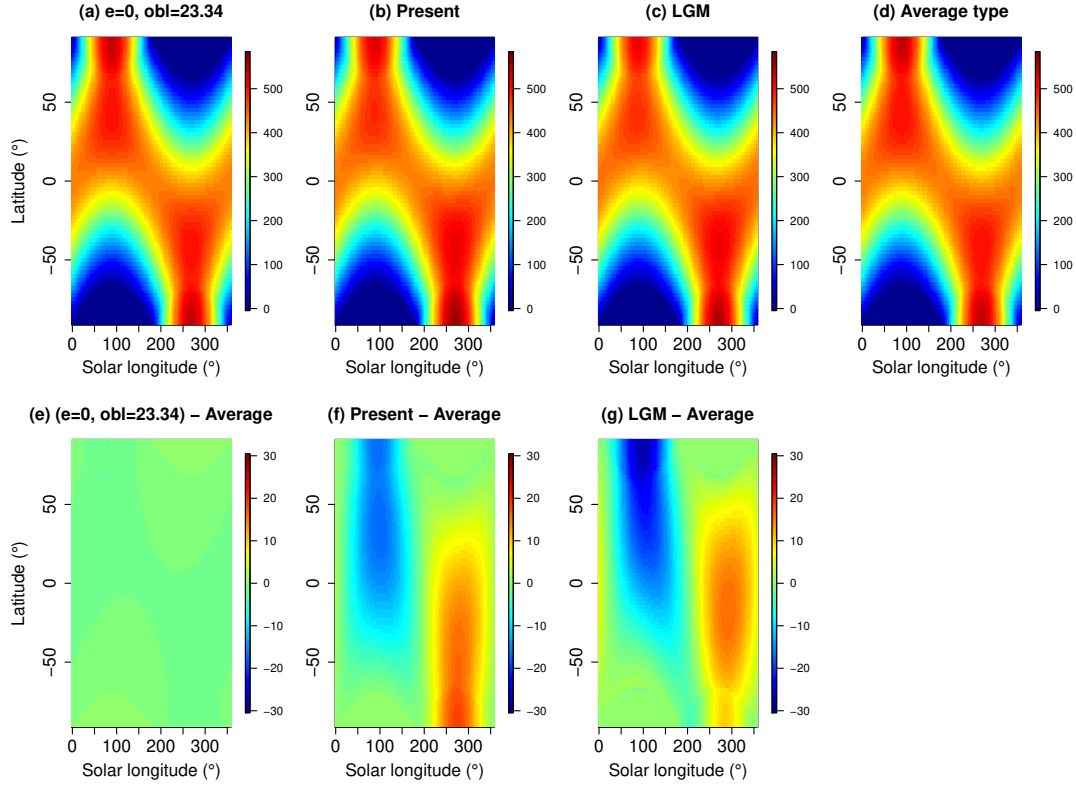


Figure S5. Seasonal insolation changes at each latitude for three different astronomical configurations. The color bar shows the daily-mean insolation [Wm^{-2}]. The horizontal axis is the true solar longitude, where 0° corresponds to the spring equinox and 90° corresponds to the summer solstice. (a) Eccentricity $e = 0$, mean obliquity $\varepsilon = 23.34^\circ$. (b) Present-day orbital configuration. (c) Last Glacial Maximum (LGM) orbital configuration. (d) Average seasonal insolation change calculated from 51 orbital configurations over the last 250 kyr sampled at every 5 kyr. (e) Seasonal insolation change for $e = 0$, $\varepsilon = 23.34^\circ$ minus the average. (f) Present-day minus the average. (g) LGM minus the average. The panels (e) to (g) indicate that the seasonal insolation change for $e = 0$ and $\varepsilon = 23.34^\circ$ is comparatively close to the average seasonal insolation change. R package palinsol version 0.93 is used for creating these plots [6].

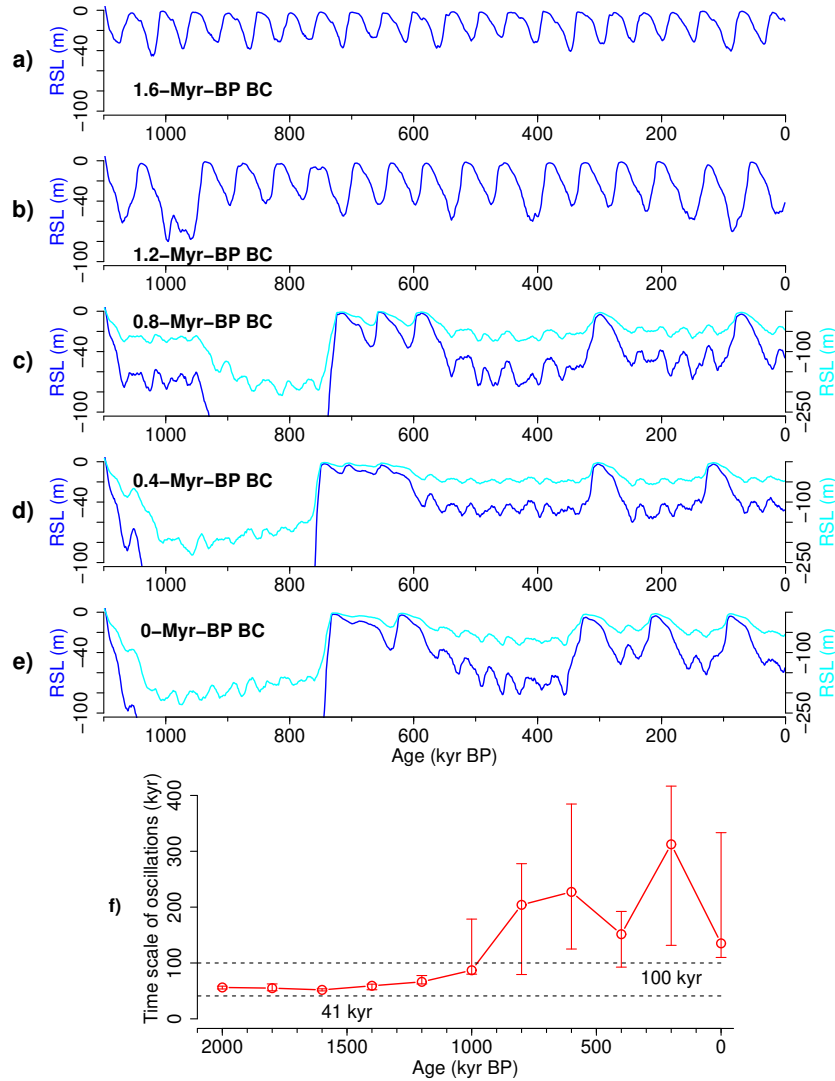


Figure S6. Increase of the time scale of internal oscillations, inferred from simulations with the present-day orbital configuration. The simulated relative sea level (RSL) for various background conditions (BC) at (a) 1.6 Myr BP, (a) 1.2 Myr BP, (c) 0.8 Myr BP, (d) 0.4 Myr BP and (e) 0 Myr BP. (f) The internal time scale as a function of age, from which the BC used for the simulation is taken. The time scale is derived from the PSD of the corresponding time series over 600–0 kyr BP, assuming that the first glacial cycle with a significantly low sea level minimum in (c) to (e) is an initial transient. The circles denote the medians and the vertical bars show the interquartile range. The horizontal dashed lines indicate 41 kyr and 100 kyr for reference. The increase of the time scale of internal oscillations is the same as Fig. 3, but it occurs in a shorter time span of a few hundred kyr.

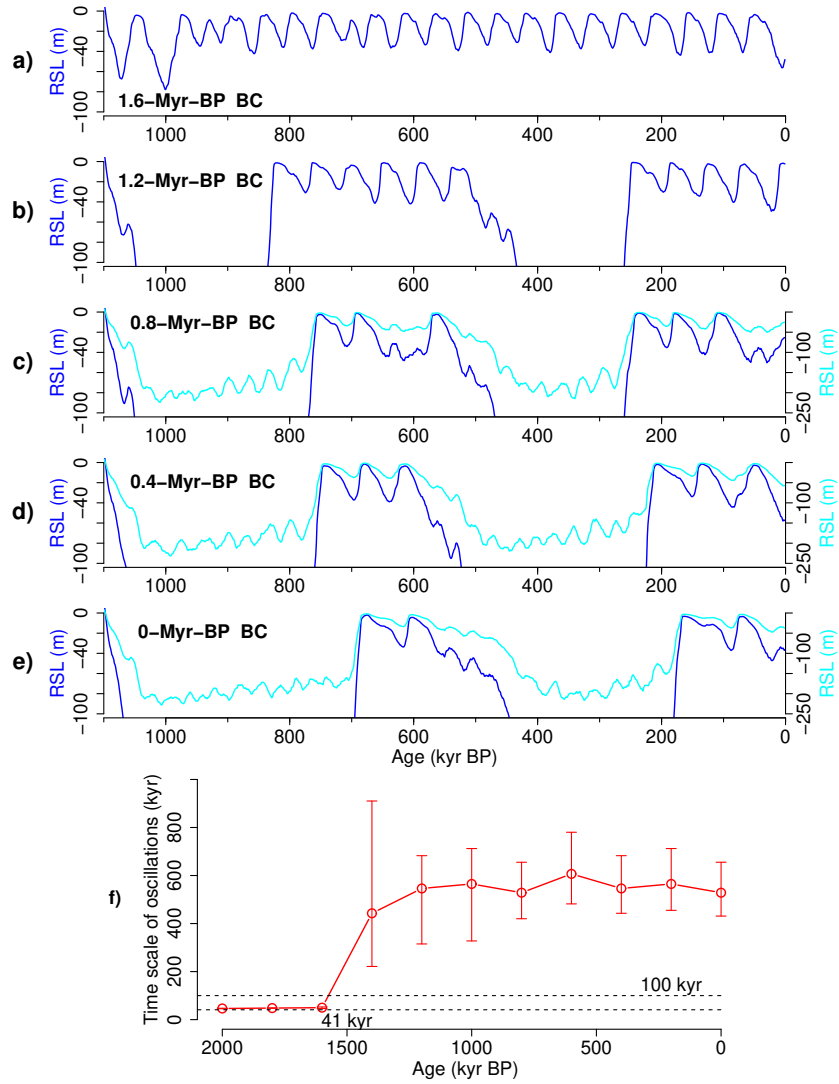


Figure S7. Increase of the time scale of internal oscillations, inferred from simulations with the orbital configuration fixed at the Last Glacial Maximum values. The simulated relative sea level (RSL) for various background conditions (BC) at (a) 1.6 Myr BP, (a) 1.2 Myr BP, (c) 0.8 Myr BP, (d) 0.4 Myr BP and (e) 0 Myr BP. (f) The internal time scale as a function of age, from which the BC used for the simulation is taken. The time scale is derived from the PSD of the corresponding time series over 1000–0 kyr BP.

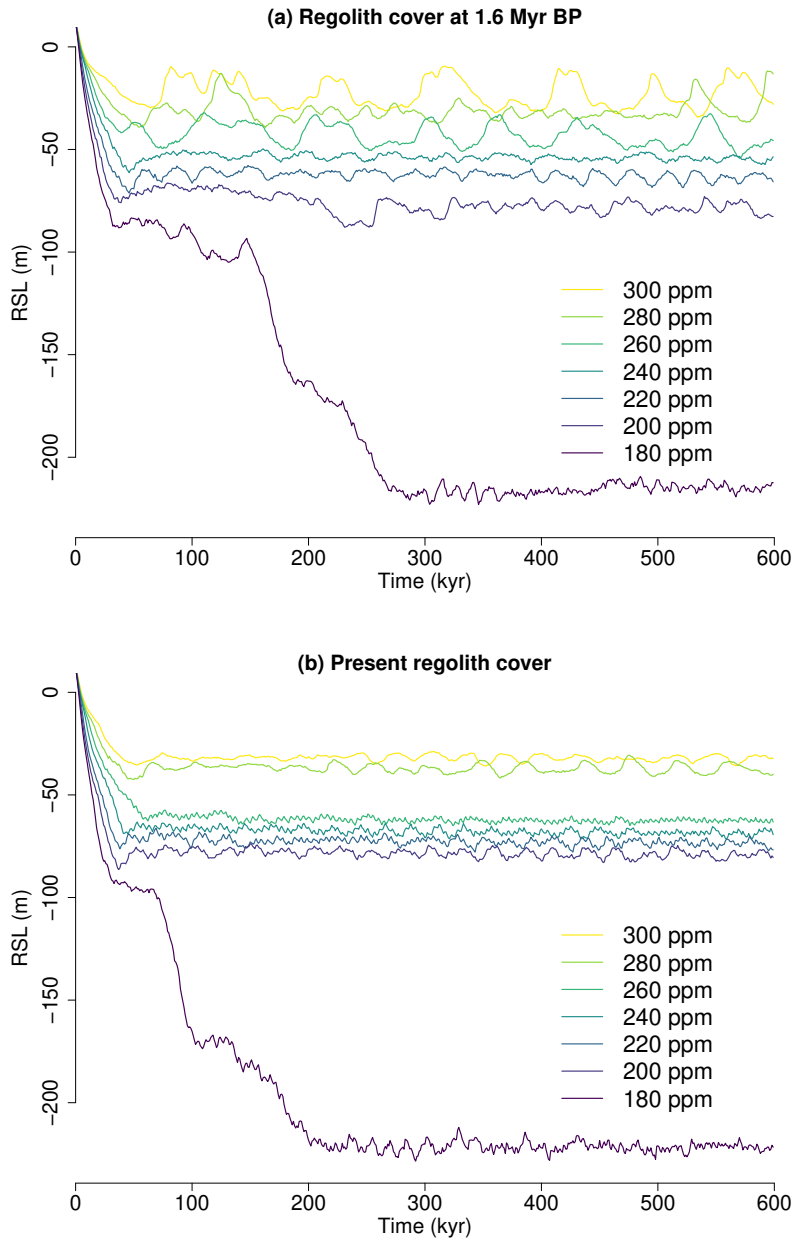


Figure S8. Relative sea levels (RSLs) simulated by CLIMBER-2 without glaciogenic dust feedback and carbon cycle feedback: (a) The case for the regolith cover at 1.6 Myr BP. (b) The case for the present regolith cover. For each simulation, a different atmospheric CO₂ concentration is prescribed.

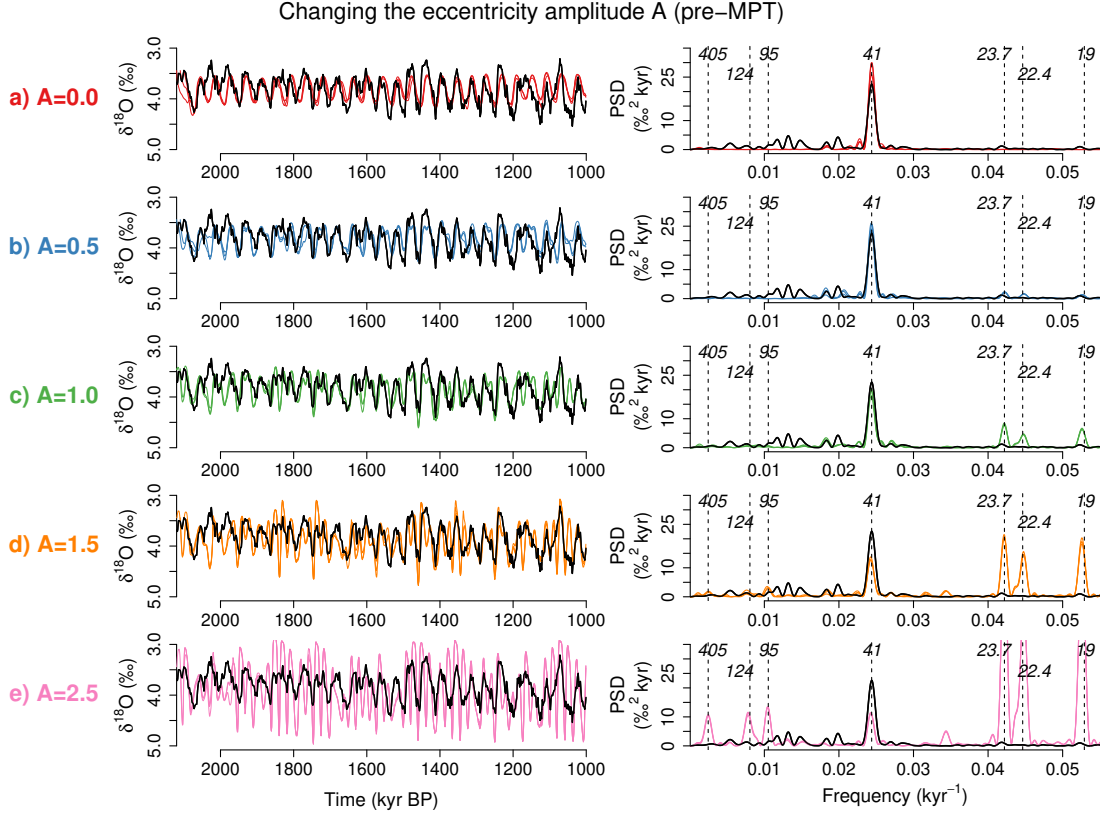


Figure S9. Sensitivity experiments changing the scale A of eccentricity [3] and climatic precession under pre-MPT (1.6 Myr BP) background condition (see text). Three simulated $\delta^{18}\text{O}$ series starting from different initial times (i.e., different orbital configurations) are shown for different values of A on the left of (a) to (e). The black line is the LR04 $\delta^{18}\text{O}$ record [2]. The corresponding power spectral densities (PSD) are shown on the right. The vertical dashed lines and italic numbers show the positions of major astronomical frequencies and their periods [3]. As A increases further than the realistic value $A = 1$, the response changes from synchronization to the 41-kyr obliquity cycles to an obedient response to the climatic precession forcing.

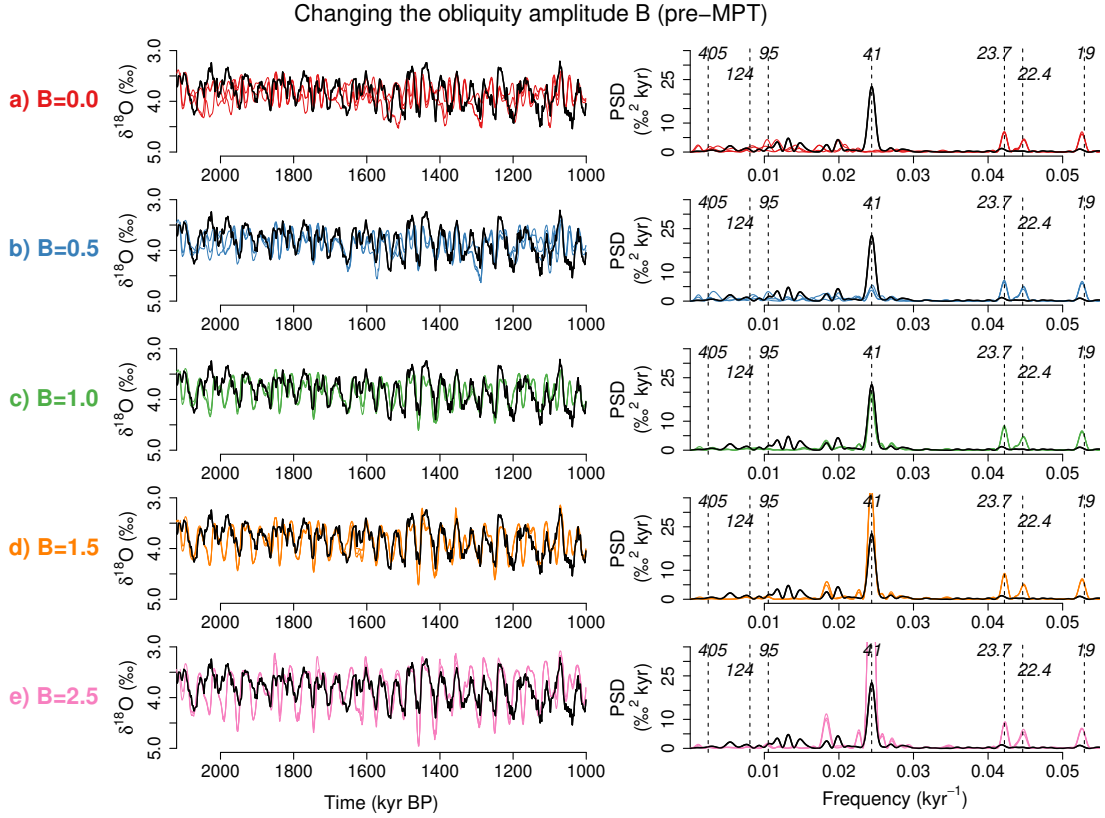


Figure S10. Sensitivity experiments changing the scale B of obliquity [3] under pre-MPT background conditions (see text). Three simulated $\delta^{18}\text{O}$ series starting from different initial times (i.e., different orbital configurations) are shown for different values of A in the left panels of (a) to (e). The black line is the LR04 $\delta^{18}\text{O}$ record [2]. The corresponding power spectral densities (PSD) are shown in the right panels. The vertical dashed lines and italic numbers show the positions of major astronomical frequencies and their periods [3]. The synchronization to the 41-kyr obliquity cycles is achieved for realistic or larger size of obliquity variations $B \gtrsim 1$.

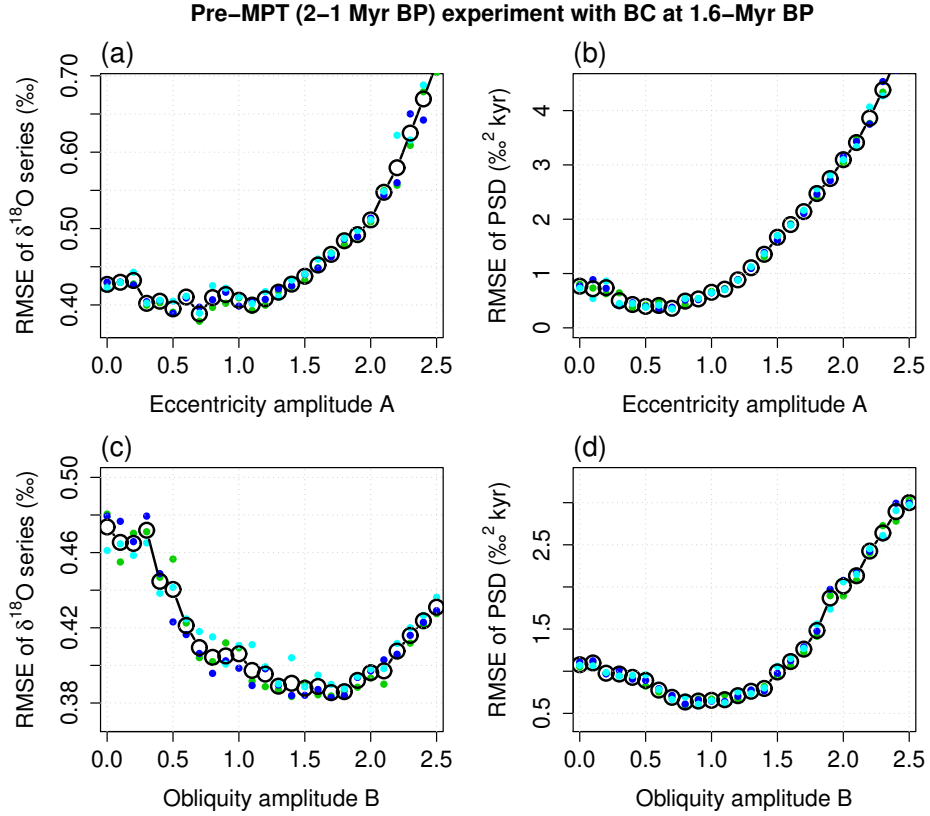


Figure S11. Comparisons between the the LR04 benthic $\delta^{18}\text{O}$ series and the model runs under the 1.6-Myr-BP background condition (BC). (a) Root mean square error (RMSE) of the actual and simulated $\delta^{18}\text{O}$ series over 2–1 Myr BP, plotted as a function of the amplitude A of eccentricity. The colored filled dots are for the three different simulations started from slightly different initial conditions (see Methods). The open circles connected with a line show the average. (b) RMSE in the spectral domain, plotted as a function of A . (c) RMSE of the actual and simulated $\delta^{18}\text{O}$ series, plotted as a function of the amplitude B of obliquity. (d) RMSE in the spectral domain, plotted as a function of B .

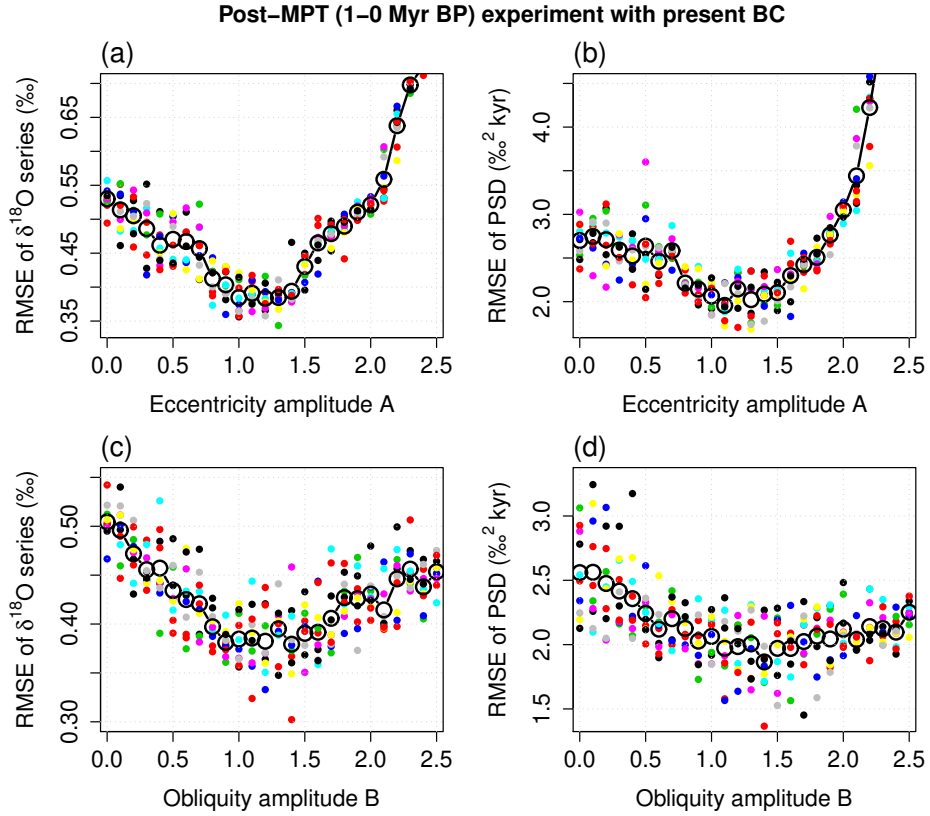


Figure S12. Comparisons between the the LR04 benthic $\delta^{18}\text{O}$ series and the model runs under the 0-Myr-BP background condition (BC). (a) Root mean square error (RMSE) of the actual and simulated $\delta^{18}\text{O}$ series over 1–0 Myr BP, plotted as a function of the amplitude A of eccentricity. The colored filled dots are for the three different simulations started from slightly different initial conditions (see Methods). The open circles connected with a line show the average. (b) RMSE in the spectral domain, plotted as a function of A . (c) RMSE of the actual and simulated $\delta^{18}\text{O}$ series, plotted as a function of the amplitude B of obliquity. (d) RMSE in the spectral domain, plotted as a function of B .

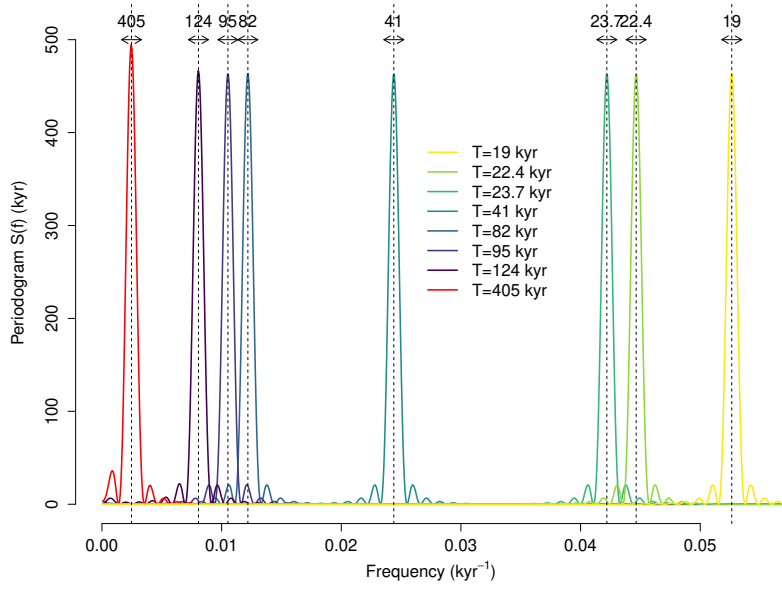


Figure S13. Power spectral density $S(f)$ of a sinusoidal wave, $\sin(2\pi t/T)$, sampled at every $\Delta t = 1$ kyr over the time interval from -1000 kyr to 0 kyr BP. The period T corresponds to major astronomical periodicities and sub-harmonics 405, 124, 95, 82, 41 and 23.7, 22.4 and 19 kyr (see main text). The vertical dashed lines and associated numbers show corresponding frequencies and periods. The arrows show the maximum frequency width $\Delta f = (1/82 - 1/95)/2 = 8.34 \times 10^{-4} \text{ kyr}^{-1}$ that is chosen to avoid any overlaps in calculating the band power corresponding to each astronomical frequency.

References

- [1] Arkady Pikovsky, Jürgen Kurths, Michael Rosenblum, and Jürgen Kurths. *Synchronization: a universal concept in nonlinear sciences*. Number 12. Cambridge university press, 2003.
- [2] Lorraine E Lisiecki and Maureen E Raymo. A pliocene-pleistocene stack of 57 globally distributed benthic $\delta^{18}\text{O}$ records. *Paleoceanography*, 20(1), 2005.
- [3] Jacques Laskar, Philippe Robutel, Frédéric Joutel, Mickael Gastineau, ACM Correia, and Benjamin Levrard. A long-term numerical solution for the insolation quantities of the earth. *Astronomy & Astrophysics*, 428(1):261–285, 2004.
- [4] Jose A Rial. Pacemaking the ice ages by frequency modulation of earth’s orbital eccentricity. *Science*, 285(5427):564–568, 1999.
- [5] Matteo Willeit, Andrey Ganopolski, Reinhard Calov, and Victor Brovkin. Mid-pleistocene transition in glacial cycles explained by declining CO_2 and regolith removal. *Science Advances*, 5(4):eaav7337, 2019.
- [6] M Crucifix. Palinsol: insolation for palaeoclimate studies, r package version 0.93, 2016.